Article

The Key Role of Carbon Materials in the Biological and Photocatalytic Reduction of Nitrates for a Sustainable Management of Wastewater

Luisa M. Pastrana-Martínez , Sergio Morales-Torres , Francisco J. Maldonado-Hódar *

Posted Date: 26 August 2025

doi: 10.20944/preprints202508.1857.v1

Keywords: biofilms; activated carbon; nanocarbons; photocatalysis; nitrate reduction; hole scavengers

 doi:10.20944/preprints202508.1857.v1

Article

The Key Role of Carbon Materials in the Biological and Photocatalytic Reduction of Nitrates for a Sustainable Management of Wastewater

Luisa M. Pastrana-Martínez, Sergio Morales-Torres and Francisco J. Maldonado-Hódar *

NanoTech – Nanomaterials and Sustainable Chemical Technologies, Department of Inorganic Chemistry, Faculty of Sciences, University of Granada, Avda. Fuente Nueva s/n, ES18071 Granada, Spain.

* Correspondence: fjmaldon@ugr.es; Tel.: +34-(958)- 240-444

Abstract

This work explores the influence of material properties and experimental conditions on both biological and photocatalytic nitrate reduction processes. For the biological route, results demonstrate that carbon supports, specifically carbon gels, with open porosity, slight acidity, and high purity enhance *E. coli* adhesion and promote the formation of highly active bacterial colonies. However, carbon supports of bacteria, produced from waste biomass, emerges as a sustainable and cost-effective alternative, improving scalability and environmental value. Complete conversion of nitrates to nitrites, followed by full nitrite reduction, is achieved under optimized conditions. Photocatalytic nitrate reduction under solar radiation is proposed also as a promising and ecofriendly upgrade method to conventional wastewater treatment. Graphene oxide (GO) was used to enhance the photocatalytic activity of TiO_2 nanoparticles for the degradation of nitrates. The efficiency of nitrate reduction is found to be highly sensitive to solution pH and the physicochemical nature of the photocatalyst surface, which governs nitrate interactions through electrostatic forces. Screening of hole scavengers revealed that formic acid, in combination with the TiO_2–GO composite, delivered exceptional performance, achieving complete nitrate reduction in just 15 minutes under batch conditions at acidic pH.

Keywords: biofilms; activated carbon; nanocarbons; photocatalysis; nitrate reduction; hole scavengers

1. Introduction

Due to their high solubility and stability, nitrates are readily transported into water resources, since they are particularly difficult to remove. As essential plant nutrients, their role in promoting algal growth and subsequent eutrophication is well documented, not only within the scientific community [1], but also among the general public. Media coverage frequently highlights ecological disasters triggered by nitrate pollution, often accompanied by shocking images of thousands of dead fish floating in affected waters. Beyond their environmental impact, nitrates and their nitrite derivatives pose serious health risks, ranging from headaches and fatigue to cancer. Because of these harmful effects, legal limits have been established to regulate their concentration in drinking water. In the United States, the Environmental Protection Agency (EPA) sets the maximum allowable nitrate concentration at 10 mg/L, European legislation is comparatively less stringent; Directive (EU) 2020/2184 sets the limit at 50 mg/L, which aligns with the World Health Organization's guideline [2]. Nevertheless, even this higher threshold is frequently exceeded in regions classified as nitrate-vulnerable zones, where groundwater contamination often forces residents to rely on bottled water instead of local supplies.

Excessive nitrate levels are typically attributed to the intensive use of fertilizers in agriculture and to manure generated by livestock farming. In Spain, for instance, the most heavily polluted

 doi:10.20944/preprints202508.1857.v1

regions are located in the southeast [1], where the Mediterranean Sea, particularly the Mar Menor, receives runoff from irrigation systems in the provinces of Murcia and Almería. These areas have experienced significant economic growth based on intensive fruit and vegetable production, driven by favorable climatic conditions. Similar issues have been observed worldwide, with recent studies highlighting comparable trends. In China [3], research indicates that the primary sources of nitrate pollution are approximately 33% from manure and sewage, 35% from chemical fertilizers, and 32% from natural sources. This means that nearly 70% of nitrate contamination is directly linked to agricultural and livestock-related activities.

Sludge carried by irrigation water is difficult to collect and it is typically discharged without treatment, except in certain hydroponic greenhouse systems. In contrast, wastewater from domestic, industrial, and often livestock sources is generally collected through sewerage systems. Domestic wastewater and farm slurry from livestock tend to exhibit similar nitrate (NO_3^-) concentrations upon entering wastewater treatment plants (WWTPs) [3]. Treatment is usually carried out through biological processes designed to degrade both organic matter and nitrates. However, numerous studies have shown that the efficiency of biological denitrification is strongly dependent on the carbon-to-nitrogen (C/N) ratio. Optimal performance is achieved at C/N ratios close to 5, whereas efficiency significantly decreases as nitrogen concentration increases, with substantial limitations observed at a C/N ratio of 2.7 [4].

To improve denitrification efficiency, external organic carbon sources can be added, but this increases both operational costs and the volume of residual waste. Furthermore, the conventional activated sludge process (ASP) is known to be energy inefficient [4,5]. To address these challenges, microbial communities can be immobilized on various types of support materials to form active biofilms. The effectiveness of these biofilms depends on the composition and morphology of the microbial communities, which in turn, are subordinate to the properties of the support materials used [6]. These biofilms are often integrated into alternative reactor designs, such as rotating drum biological contactors (RDBCs), to enhance treatment performance [7].

Alternative denitrification methods involve physical, chemical, and catalytic approaches [8]. Physical processes include techniques such as reverse osmosis, ion exchange, electrodialysis, and electroreduction. Each of these methods has specific advantages and limitations that must be evaluated individually. Common challenges associated with physical treatments include high energy consumption, membrane fouling, and the need for frequent maintenance. Chemical reduction represents another promising strategy, particularly the use of zero-valent iron (Fe^0) in acidic media to reduce nitrate. This approach is attractive due to the low cost and widespread availability of iron. However, this reaction is highly pH dependent, being fast at pH = 2 but slow at pH = 3, requiring constant replacement of the consumed acid. At neutral or basic conditions, Fe is deactivated with the formation of iron oxides. On the other hand, considering other environmental aspects, Fe^{2+} is formed in solutions, which must also be adsorbed or precipitated before casting, thus adding cost and additional steps, while NH_3 emissions are also produced (Eq. 1), depending on the solution conditions.

$$4Fe^0 + NO_3^- + 9H^+ \rightarrow 4Fe^{2+} + NH_3 + 3H_2O \quad \Delta G^º = -942 \frac{KJ}{mol} \tag{1}$$

$$5Fe^0 + 2NO_3^- + 12H^+ \rightarrow 5Fe^{2+} + N_2 + 6H_2O \quad \Delta G^º = -797 \frac{KJ}{mol} \tag{2}$$

Different catalytic approaches have also been explored for the reduction of nitrates in aqueous solutions. Cai et al. [9] investigated the electrochemical reduction of nitrate to nitrogen (N_2) using a two-electrode system with Pd–Cu supported on mesoporous carbon as the cathode catalyst. This method enables the effective reduction of highly concentrated nitrate solutions (up to 650 mg L^{-1}), avoiding the limitations associated with biological treatments.

Photodegradation of nitrates was first reported by Kudo et al. in 1987 using Pd-TiO_2 as a catalyst [10]. In general terms, nitrate reduction can be described as consecutive reactions where nitrates are

 doi:10.20944/preprints202508.1857.v1

reduced to nitrites which can be finally converted to nitrogen or ammonium. In order to improve the rate of photoreduction reactions, hole scavengers are often added to the reactant mixture to limit the formation of oxidant species. The nitrate reduction is sensitive to pH, hence an effective pH regulation is necessary during the reaction, since basic conditions significantly promote the formation of ammonium ions [11,12]. In acid media reaction develops following the progressive reduction as:

$$NO_3^-(aq) + 2e^- + 2H^+(aq) \rightarrow NO_2^-(aq) + H_2O(l) \quad (3)$$

$$2NO_2^-(aq) + 6e^- + 8H^+(aq) \rightarrow N_2(g) + 4H_2O(l) \quad (4)$$

$$NO_2^-(aq) + 6e^- + 8H^+(aq) \rightarrow NH_4^+(aq) + 2H_2O(l) \quad (5)$$

While in basic media:

$$NO_3^-(aq) + 2e^- + H_2O(l) \rightarrow NO_2^-(aq) + 2OH^-(aq) \quad (6)$$

$$2NO_2^-(aq) + 6e^- + 4H_2O(l) \rightarrow N_2(g) + 8OH^-(aq) \quad (7)$$

$$NO_2^-(aq) + 6e^- + 6H_2O(l) \rightarrow NH_4^+(aq) + 8OH^-(aq) \quad (8)$$

Photocatalytic reduction also offers additional advantages, notably the absence of reagent consumption [8,13], thus avoiding the careful maintenance of the experimental conditions in Fe-based reductions. The preparation method of the photocatalyst (TiO_2) strongly determines its performance [14]. Several parameters should be controlled. The anatase phase is more active than the rutile phase in nitrate degradation, achieving high conversions with 100% selectivity to N_2 [15]. The synthesis of nano-sized TiO_2 and doping with Pd have also been proposed as effective tools to enhance the degradation of nitrate species under UV (365 nm) irradiation [12,13]. From a sustainability perspective, the reaction becomes significantly more attractive when solar light is used as the energy source, eliminating the need for external energy input. In this context, composites of TiO_2 with carbon-based materials, such as graphene oxide (GO), offers several benefits over noble metal dopants [16]. These include reduced material costs, lower corrosion susceptibility, and improved charge separation due to the donor–acceptor properties and light sensitization effects of the carbon phase.

The development of sustainable technologies that ensure safe drinking water while being easily implemented at pollution sources, such as farms, agri-food facilities, or, in severe cases, as an upgrade to existing wastewater treatment plants (WWTPs), remains a key scientific challenge. To improve both sustainability and practical deployment, this work explores two complementary strategies for nitrate removal: (1) the use of low-cost, biomass-derived activated carbons (ACs) to enhance biologically active biofilms, and (2) the synthesis of nanocomposites of TiO_2 with carbon nanomaterials (GO) with unique reactivity under solar light. Experimental conditions, such as pH and the application of scavengers, were optimized to maximize nitrate reduction. The results demonstrate that both biological and photocatalytic approaches can be significantly improved to achieve complete conversion of nitrate to nitrogen gas (N_2) in solution.

2. Materials and Methods

2.1. Synthesis of Carbon Materials and TiO_2-GO Composites

Three carbon materials with different origins and properties were evaluated as support for *E. coli* bacteria. The first material, a carbon xerogel (CA), was synthesized from resorcinol–formaldehyde (R–F) mixtures via sol–gel polymerization. The resulting gel was dried in an oven at

 doi:10.20944/preprints202508.1857.v1

atmospheric pressure (100 °C, overnight) and subsequently carbonized at a relatively low temperature (500 °C). The synthesis procedure has been described in detail in previous work [17]. The second material, denoted as A sample, was derived from almond shells. These were initially carbonized at 800 °C, followed by activation under a CO_2 atmosphere for 4 hours to enhance porosity. The third carbon support, referred to as N sample, served as a commercial reference. It is an acid-washed, steam-activated carbon with a high pore volume, commercially available under the name RX3-Extra from Norit.

TiO_2 and TiO_2–GO catalysts were prepared and used in the photocatalytic reduction of NO_3^-. GO was obtained from an aqueous dispersion of graphite oxide (prepared by the modified Hummers method) with subsequent dispersion in an ultrasonic bath [18,19]. The TiO_2–GO compound was synthesized with this GO dispersion by the sol-gel method with an optimum GO content of about 4 wt.% and 200 °C (in N_2 atmosphere) as previously described [19]. Briefly, ammonium hexafluorotitanate (IV), $(NH_4)_2TiF_6$ (0.1 mol/L), and boric acid, H_3BO_3 (0.3 mol/L) were added to the GO dispersion (1 gL^{-1}) and heated at 60 °C for 2 h under stirring. The GO loading was fitted at ca. 4 wt.% where the optimal assembly and interfacial coupling of the TiO_2 nanoparticles with the GO sheets was reached [19]. Bare TiO_2 was also prepared by the same method, without adding any carbon material. The commercial P25 was also studied for comparative purposes.

2.2. Characterization Techniques

Textural characterization of samples was carried out by physical adsorption of N_2 at −196 °C using a Quantachrome Autosorb-1 equipment. From the isotherm data, parameters such as the BET surface area (S_{BET}) and the volume (W_0), surface (S_{micro}) and width (L_0) of micropores were estimated by applying Brunauer-Emmett-Teller, Dubinin–Radushkevich and Stoeckli equations, respectively [20-22]. The total pore volume (V_T) was considered as the volume of N_2 adsorbed at $P/P_0 = 0.95$. The point zero of charge (pH_{PZC}) of the powder materials was determined following a pH drift test. Solutions with varying initial pH were prepared using HCl or NaOH and 50 mL of NaCl as electrolyte containing 0.15 g of the material. The PZC value of the material was determined by intercepting the obtained final-pH vs. initial-pH curve with the straight line final-pH = initial-pH [23]. Thermogravimetric (TG) analysis of the composites was obtained using a SHIMADZU TGA–50H thermobalance by heating the sample in air flow up to 950 °C with a heating rate of 20 °C min^{-1}. The crystalline properties of photocatalysts were determined by XRD (PANalytical X'Pert MPD) and the analysis of the bandgap by spectroscopic DRUV-Vis experiments (UV-Vis JASCO V-560). The spectra have been collected in diffuse reflectance mode and subsequently transformed into equivalent Kubelka-Munk absorption units. Scanning microscopy, SEM-images, were recorded with a LEO (Carl Zeiss) model GEMINI-1430-VP to analyze the morphology of the samples as well as the architecture of the bacteria forming the biofilm.

2.3. Nitrate Removal

2.3.1. Biological Treatment

Bacteria used in the experiments was *Escherichia Coli*, ATCC® 25922™ strain, which was first incubated at 37 °C using a buffered media at pH 7 with tryptic soy broth (TSB) before being immobilized on the different supports. Bacteria were supported on the different solids adding 1 ml of this suspension to 0.4 g of support suspended in 20 mL of TSB and the mixtures were shaken at 37 °C for 3 days. Afterward, the colonized supports were filtered and washed repeatedly with sterilized distilled water.

The denitrification process of water was studied by bacteria immobilized on the different supports (0.2 g), which were added to 100 mL of a solution containing 10 mg L^{-1} of nitrate from $NaNO_3$ and 1.3 mL of ethanol. The suspension was buffered at pH 7 with an appropriate phosphate solution. The flasks used as batch bioreactors were flushed with argon atmosphere to obtain anaerobic conditions and then, placed in a thermostatic rotary shaker at 25 °C. Periodically, the

 doi:10.20944/preprints202508.1857.v1

concentration of nitrate was measured directly in the bioreactors with a selective electrode supplied by Mettler, and simultaneously, a small volume of solution (1 mL) was withdrawn for the determination of the nitrite concentration. This parameter was determined using a Hitachi model U2000 spectrophotometer at 543 nm after coupling diazotized sulphanilamide with N-1-naphthyl-ethylendiamine [24].

2.3.2. Photocatalytic Reduction of Nitrate

The photocatalytic reduction of nitrate of nitrate was performance under simulated solar radiation at room temperature (average 25 °C) using a SOLAR BOX 1500e (CO.FE.MEGRA, Milano) provided with a 1500 W Xenon lamp (500 W m^{-2} of irradiance power). The photochemical reactor consists in a glass reactor loaded with 100 mL of solution containing the nitrate solution (50 mg L^{-1}). The catalyst concentration was fixed as 0.5 g L^{-1}. The suspension was magnetically stirred under nitrogen stream to displace possible dissolved oxygen and allowing to establish the adsorption equilibrium on the catalysts (dark phase). Aliquots were collected at specific time intervals (5, 15, 30 and 60 min) and filtered with 0.45 μm cellulose acetate filters before determining the nitrate concentrations and the nitrite ions by ion chromatography (LC-10A, Shimadzu, Japan). The content of NH_4^+ was analyzed according to the standard colorimetric method (Nessler's reagent).

The experiments to determine the effect of pH and the nature of the hole scavenger (0.08 M) in photocatalysis were conducted using the same methodology previously described, with the pH adjusted prior to the dark phase to the values (2.5, 4.0, 7.5 and 10.0) using diluted HCl for acidic conditions and diluted NaOH for basic conditions, measured with a pH meter (CRISON micropH 2002). The photocatalytic reduction of nitrate was studied in presence of formic acid (HCOOH), oxalic acid ($C_2H_2O_4$) or ethanol (EtOH) as hole scavengers, respectively. Formic acid was selected to study the effect of scavenger concentration at 0.04, 0.08, and 0.12 M.

3. Results and Discussion

3.1. Biological Treatment

3.1.1. Materials Characterization

Three different carbon materials (carbon xerogel, CA; bio-ACs, A; and commercial ACs, N) were selected to develop *E. coli* biofilms for nitrate decomposition. Samples were selected trying to cover a wide range of properties, in order to obtain correlations between the performance of biofilms and textural and chemical properties of substrates.

ACs are versatile materials widely used for water treatments. They can be produced from various precursors under different synthesis conditions. The characteristics of ACs depend on both the raw materials and the treatment conditions. As a result, a wide variety of materials can be obtained, differing in the amount of inorganic impurities (ash content), degree of graphitization, surface functionalization, and porosity. To obtain cost-effective materials and enhance the sustainability of wastewater treatments (WWTs), we selected almond shells as the precursor for one of the ACs used as a bacterial support. Almond shells are an abundant and inexpensive biomass waste, particularly in Mediterranean countries. They typically consist of 38.48% cellulose, 28.82% hemicellulose, and 29.54% lignin and after carbonization and activation present a low content of inorganic matter.

In contrast, carbon aerogels (CA sample), prepared from pure reactants (RF), are consequently more expensive materials, but they are free of inorganic components, and their porosity can be designed to favor macro, meso or microporosity by fitting different parameters of synthesis during polymerization, drying and carbonization processes [17].

The carbonization processes of both precursors were simulated using a thermobalance, in which a small amount of each precursor was heated under a N_2 flow at a rate of 10 °C/min up to 800 °C (slow pyrolysis). Figure 1 shows the TG-DTG profiles obtained for the carbonization of the lignocellulosic

 doi:10.20944/preprints202508.1857.v1

material (almond shells, denoted as AS) and the raw RF polymer (xerogel). The decomposition of commercial pure microcrystalline cellulose (denoted as MCC) was also included as a reference.

As observed, MCC decomposes in a single step, with only one peak appearing in the DTG profile at around 360 °C. The TG profile of AS initially shows a weight loss due to moisture desorption, followed by the decomposition of hemicellulose. The TG curve begins to decrease at lower temperatures but with a moderate slope compared to MCC, indicating interactions between the different biomass components. The maximum decomposition rate occurs at approximately 375 °C (DTG profile), confirming that cellulose is the main component. Cellulose decomposition is complete at around 400 °C. After this point, the slope of TG-profile decreased again, associated to the greater stability of the lignin phase. The average yield of biochar obtained at 800 °C from AS in various batch furnace experiments is around 18%. In this case, the sample from almond shell tested as bacteria support was thereafter activated, undergoing an additional weight loss of 28%.

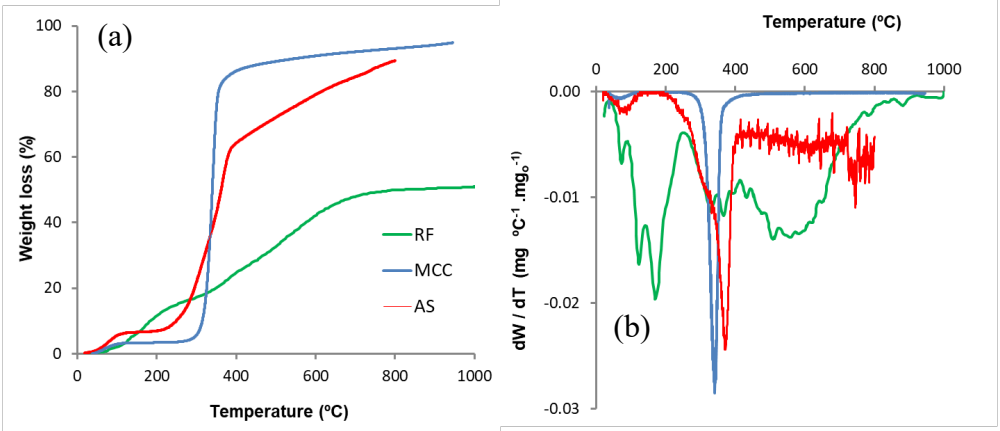

Figure 1. (**a**) TG and (**b**) DTG-profiles obtained during the carbonization of lignocellulosic and poymeric RF precursors.

The TG-DTG profiles obtained during the carbonization of RF polymers are evidently very different than those discussed for biomass pyrolysis. The decomposition of the chemical structure of the polymers is associated to two main processes, the breakage of C-O bonds and C-C at around 350 and 550 °C respectively [17,25], carbonization being complete at around 700 °C. Desorption at low temperature (below 200 °C) is mainly associated with the removal of solvents. At a glance, the first conclusion observed is that the proportion of residue increases. The carbonization of RF polymers yields around 50% wt. of char at 800 °C regarding 18% obtained from biomass residues. This fact can partially compensate for the cost of production of the different materials.

The physicochemical properties of the samples tested are summarized in Table 1. As expected, the CA sample is a pure carbon material with negligible ash content. Among the ACs, the A sample (prepared almond shells) shows a relatively low ash content compared to the commercial N sample. The CA sample (carbon xerogel), produced at a lower temperature and without activation, exhibits a lower pHpzc, indicating weakly acidic behavior. In contrast, both ACs display a markedly basic character.

Table 1. Textural properties and pH_{PZC} of the materials.

Support	*Ash* (% wt.)	pH_{PZC}	S_{BET} ($m^2\ g^{-1}$)	V_{total} ($cm^3\ g^{-1}$)	W_0 ($cm^3\ g^{-1}$)	L_0 (nm)	V_{meso} ($cm^3\ g^{-1}$)
CA	null	6.3	594	0.69	0.21	2.5	0.48
A	0.3	10.6	913	0.47	0.32	1.4	0.15
N	4.8	11.0	1233	0.60	0.56	1.5	0.04

S_{BET} = BET surface area, V_T = total pore volume, W_0 = micropore volume L_0= mean micropore width, V_{meso} = V_T-W_0 mesopore volume, obtained by difference according to the Gurvich rule.

 doi:10.20944/preprints202508.1857.v1

From a textural point of view, the most notable differences are also observed between CA and the ACs, as clearly shown by the shapes of their N_2 adsorption isotherms (Figure 2). Both AC samples exhibit Type I isotherms, typical of predominantly microporous materials. In contrast, the CA sample displays a Type IV isotherm with a pronounced hysteresis loop, indicating a mesoporous structure. Consequently, the ACs exhibit well-developed microporosity (W_0) and higher surface area values compared to CA (Table 1). However, the total pore volume (measured by the volume of liquid nitrogen adsorbed at $P/P_0 = 0.9$, Figure 2) and the mesopore volume are both higher in the carbon aerogel sample.

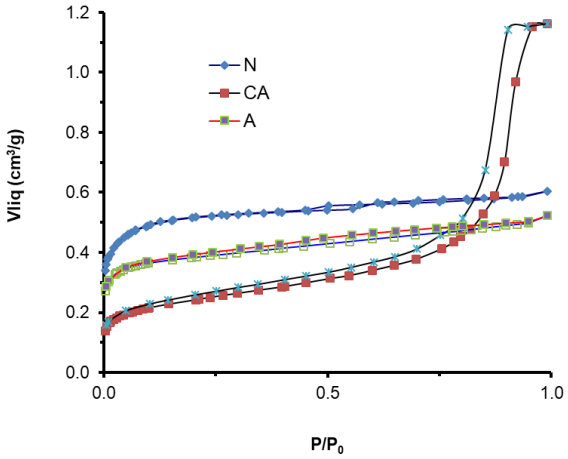

Figure 2. N_2 adsorption–desorption isotherms of carbon xerogel, CA; bio-ACs, A; and commercial ACs, N.

3.1.2. Performance of Adhered Biofilms

The performance of *E. coli* biofilms in nitrate removal, when supported on the various carbon materials, is presented in Figure 3. Control experiments conducted in the absence of microorganisms showed that nitrate adsorption or degradation by the carbon supports alone was negligible. Regardless of the carbon material used, the nitrate concentration remained stable. Therefore, the decrease in nitrate concentration observed after immobilizing the biofilms on the supports can be attributed solely to the bacterial activity involved in the nitrate reduction process.

It is well known [26] that the reduction of NO_3^- by bacteria occurs following a four-step process: microorganisms reduce nitrates NO_3^- progressively to nitrites NO_2^-, nitric oxide NO, nitrous oxide N_2O, and finally to nitrogen gas N_2. In this study, gas-phase analysis was not performed; instead, only the evolution of species in solution (nitrate and nitrite) was monitored.

Figure 3a shows the kinetics of NO_3^- reduction by *E. coli* biofilms supported on pure carbon aerogels (CA), compared with those supported on activated carbons (N and A). The subsequent degradation of nitrite intermediates by the different biofilms is presented in Figure 3b. It is noteworthy that both nitrates and nitrites were completely reduced and eliminated from the aqueous solution by the *E. coli* biofilms, regardless of the nature of the carbon support. However, the biofilm developed on CA exhibited higher activity than those formed on the ACs, resulting in faster reduction of both nitrate and the subsequent nitrite. The concentration of NO_2^- increased as NO_3^- decreased, indicating a sequential reduction pathway. Because of the imposed anaerobic conditions, bacteria exhibit a higher affinity for NO_3^- than for NO_2^-, such that the concentration of NO_2^- does not begin to decrease until NO_3^- is almost completely depleted. Once NO_3^- is consumed, bacteria proceed to reduce NO_2^- completely. Initially, the concentration of NO_2^- is zero, but it increases as the reaction progresses. This behavior suggests a mechanism involving the adsorption of NO_3^- onto the biofilm surface, followed by desorption of NO_2^- while nitrate remains readily available in the medium. This confirms the role of NO_2^- as a reaction intermediate. It also implies that the adsorption of NO_3^- is faster and energetically more favorable than its immediate reduction. If reduction occurred directly

 doi:10.20944/preprints202508.1857.v1

on the adsorbed NO_3^- without desorption, no accumulation of NO_2^- in the solution would be observed.

Interestingly, the curves in Figure 3b are nearly symmetrical, indicating that the rates of NO_2^- formation and subsequent reduction are relatively similar. The lower affinity of the biofilms for NO_2^- also accentuates differences in biofilm activity: broader curves correspond to slower nitrite formation from nitrate and slower subsequent reduction to N_2.

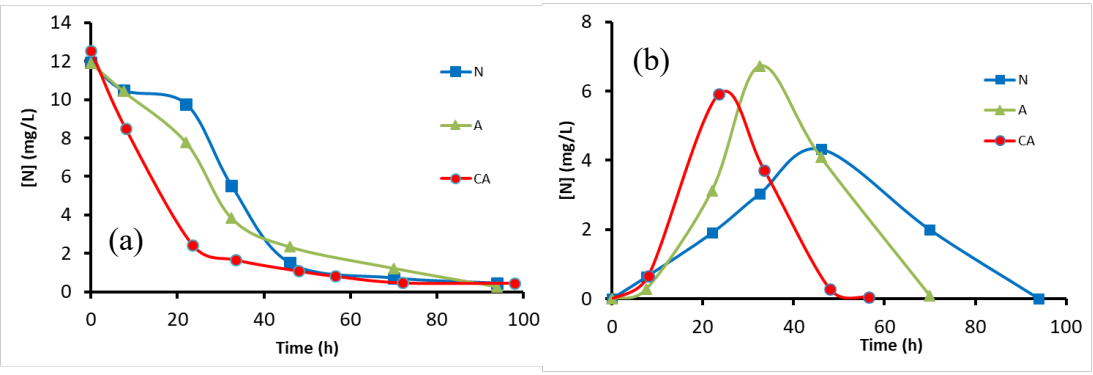

Figure 3. Comparison of the denitrification activity of E. Coli colonies deposited on carbon aerogels and activated carbons. (**a**) Reduction of NO_3^- to NO_2^-; (**b**) Formation and posterior reduction of NO_2^- in solution.

The morphology of the bacteria colonies in supported biofilms was analyzed by SEM (Figure 4). On the CA sample, bacteria tend to cluster together, while in the case of the activated carbons (ACs), they appear more dispersed. In both the CA and A samples, bacteria are connected to each other and to the carbon surface through excreted fibers, which are less frequently observed in the N sample. These filaments are biosynthesized polysaccharides and may play a role in electron transfer processes [27], potentially influencing the redox activity of the bacteria.

Since the incubation of *E. coli* on the various supports was conducted in buffered solutions at pH = 7, the AC surfaces would be positively charged. This condition is generally favorable for interaction with *E. coli*, a Gram-negative bacterium [28]. Nevertheless, more structured colonies were observed in CA.

Although all biofilms were capable of completely removing the initial nitrate load, the differences in performance are likely related to the distinct characteristics of the supports that influence biofilm architecture. When correlating the physicochemical properties of the supports with colony morphology and denitrification performance, it becomes evident that the best results—specifically, the fastest NO_3^- reduction kinetics—are achieved with biofilms supported on the mesoporous, pure carbon CA sample, in comparison with those supported on ACs. The porous structure and surface chemistry of the support materials influence bacterial interaction and biofilm formation. The open, coral-like mesoporous structure of the CA sample provides surface irregularities and roughness that facilitate bacterial anchoring. Given that nitrate adsorption onto the supports is negligible and that micropores are inaccessible to bacteria due to their size, the highly microporous surfaces of the ACs seem to have limited influence on biofilm performance. As showed in previous works [29], some oxygenated functionalities (-OH, -COOH, -CHO, or -C=O), can form hydrogen bonds with bacterial cell walls, promoting attachment to the carrier surface. The lower carbonization temperature used for the CA sample likely preserves a higher concentration of such oxygenated surface groups (OSG). Comparing the performance of ACs, both present a marked basic character, but sample A present a certain mesopore volume and lower ash content than sample N. This led to an intermediate character between CA and N samples, thus showing poorly structured colonies as on N but bacteria are attached to the carbon surface by filaments as on CA. In a previous work [30], we demonstrated that doping carbon gels with different metal oxides (SiO_2, TiO_2, Al_2O_3) progressively limit the activity of *E. coli* biofilms as the acidic character of the oxide increases. This could help explain the lower performance observed for sample N.

 doi:10.20944/preprints202508.1857.v1

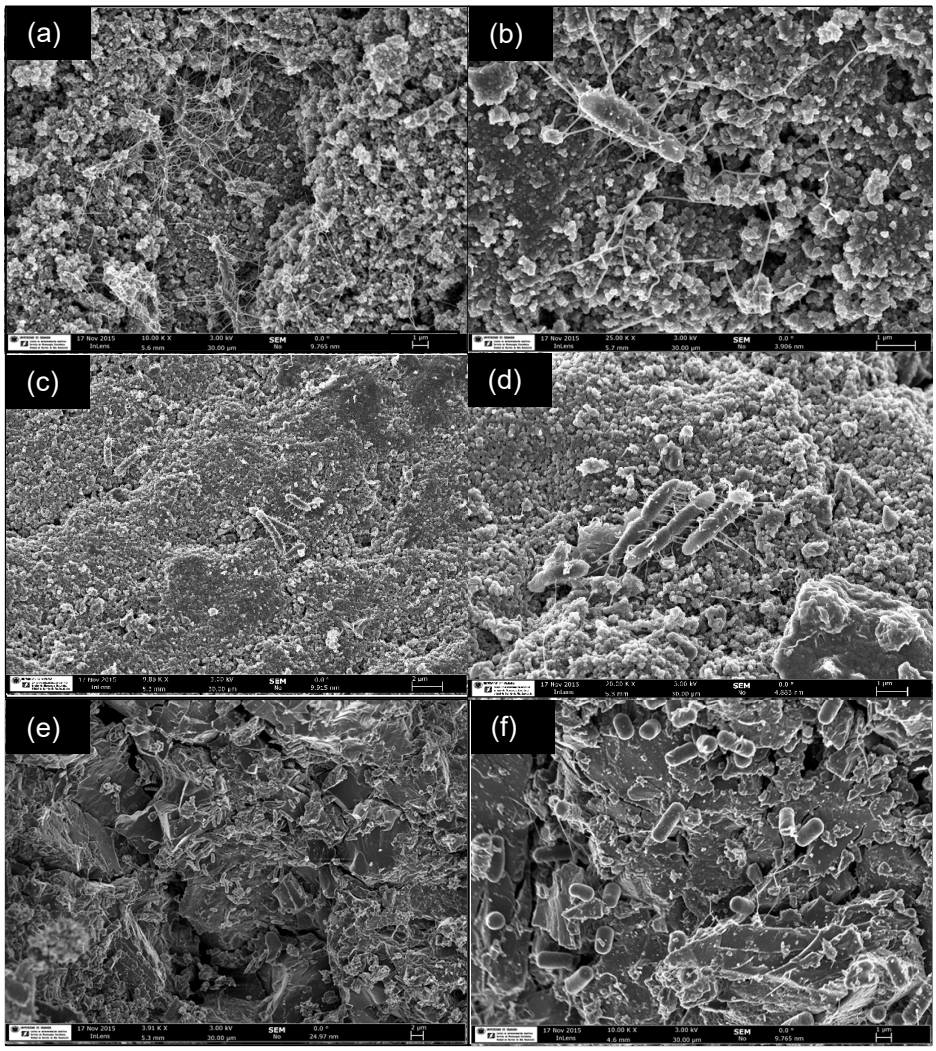

Figure 4. SEM micrographs of of the biofilms supported on (**a, b**) carbon aerogels, (**c, d**) A- activated almond shells and (**e, f**) N-commercial ACs from Norit.

The best biofilm performance was observed when *E. coli* was supported on the CA material, which can be attributed to its neutral or slightly acidic surface character, mesoporous structure, and absence of impurities. Furthermore, the presence of oxygen-containing surface functionalities can further enhance the formation of active bacterial colonies. Additional advantages of the use of carbon gels are related to the proper sol-gel process, which allows for the incorporation of heteroatoms or metallic phases into the carbon matrix, enabling precise tuning of surface hydrophobicity and electrochemical behavior.

Moreover, to reduce reactant consumption, carbon gels can be synthesized as thin films deposited on various supports. Once the optimal combination of pore structure and surface chemistry is established, different types of monolithic ceramic structures (e.g., honeycombs, foams) can be coated using spin or dip-coating techniques with an appropriate mixture of reactants [31,32]. Polymerization and carbonization are then carried out on the impregnated monoliths. This process yields stable, thin films, while the open channels of the monoliths facilitate wastewater diffusion without significant mass transfer limitations, even under atmospheric pressure or in the presence of fouling. Using biomass as a precursor is also a promising and cost-effective approach to produce materials with excellent properties for biofilm support. Based on the results discussed, biochar can serve as an effective alternative to ACs, eliminating the need for the activation step and thereby saving time, energy, and chemicals. The potential of biochar as a bacterial support has been recently reviewed [33]. The authors concluded that biochar could contribute to improved performance of the biofilm through various mechanisms, including electron transfer, microbial immobilization or

 doi:10.20944/preprints202508.1857.v1

alterations in microbial structure at the genetic level. Many different modifications of biochar, namely doping coconut biochar with humid acid, improve the nitrate removal of bioreactors around 33% [34].

A key advantage of carbon materials lies in their versatility with a wide variety of available precursors, along with multiple carbonization, activation, and functionalization strategies, providing a broad design space for tailoring properties. This flexibility often results in materials that are more cost-effective than other commonly used supports or adsorbents, including inorganic oxides, zeolites and metal–organic frameworks (MOFs).

3.2. Photocatalytic Reduction of Nitrates

3.2.1. Catalyst Characterization

Table 2 summarizes the surface area (S_{BET}), crystalline phases, point of zero charge (pH_{PZC}), band-gap energies (Eg) for the photocatalysts tested.

The TiO_2 nanoparticles synthesized exhibited an acidic surface character, with a pH_{PZC} around 3.5, which is attributed to the nature of the precursor employed during synthesis. Similarly, the TiO_2–GO composite showed a slightly lower pH_{PZC} value, likely influenced by the incorporation of GO. In contrast, the commercial P25 material showed an almost neutral surface with a pH_{PZC} close to 6.5. The functionalities of materials were analyzed by FTIR (Figure 5a) that confirms the purity of the phases as well the interplay of both phases in the composite. In both TiO_2 and the TiO_2-GO composite, the typical band between 800-950 cm^{-1} corresponding to the Ti-O-Ti bond is observed. The most characteristic absorption bands of GO correspond to the vibration bands of the C-OH groups located around 3000-3500 cm^{-1}, carbonyl groups (C=O) at 1720 cm^{-1}. At 1250 cm^{-1} and at 1050 cm^{-1} are observed the characteristic bands corresponding to the tension vibration mode of C-OH and ether C-O-C groups, respectively. It is noteworthy that the intensity of the peak associated with the hydroxyl and ether groups decreases notably in TiO_2-GO, suggesting possible bonds of TiO_2 with the surface groups of GO at these positions.

XRD patterns (Figure 5b) of both TiO_2 and TiO_2–GO showed only the peak distribution associated to the anatase phase, although the presence of GO in the composite seems to increase the crystallinity of the oxide, resulting in narrower peaks. No GO peaks were detected in the diffractogram of the TiO_2-GO composite. XRD patterns of P25 (not shown) confirm the well-known presence of both anatase-rutile crystallographic phases in this sample.

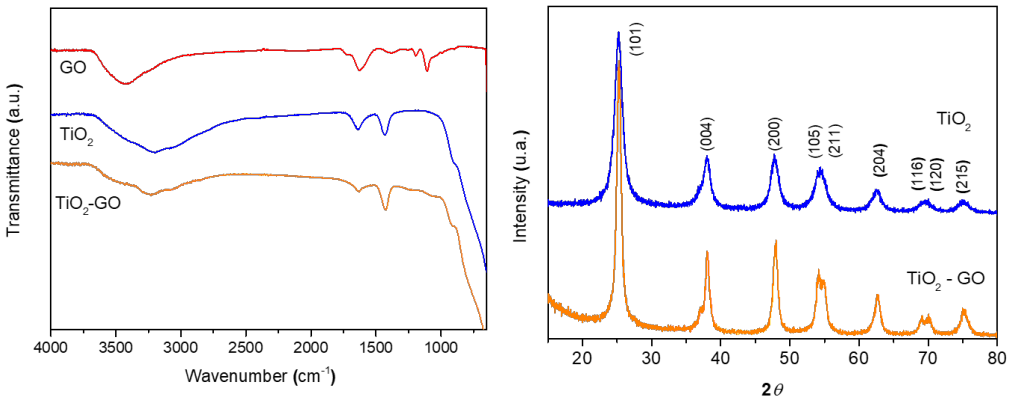

Figure 5. (**a**) FTIR and (**b**) XRD diffraction patters of TiO_2 and TiO_2-GO.

Together structural and chemical properties, textural properties are also involved in the adsorptive performance of the samples (Table 2). In terms of surface area, TiO_2 and TiO_2–GO showed significantly higher S_{BET} values (118 and 120 $m^2\ g^{-1}$, respectively), consisting of anatase-phase particles with average crystallite sizes of 8 nm for TiO_2 and 4 nm for TiO_2–GO. On the other hand, P25 showed a lower surface area of 52 $m^2\ g^{-1}$ and a mixture of anatase and rutile phases (85 and 15% of anatase

 doi:10.20944/preprints202508.1857.v1

and rutile, respectively). The porosity analysis suggests that P25 primarily contains macropores or interparticle voids, as indicated by its Type II nitrogen adsorption isotherm. In contrast, the TiO_2–GO composite exhibit mesoporous or even microporous characteristics, owing to the structural influence of GO, as previously reported [19].

The photocatalytic performance is directly related with the interaction of the samples with the radiation, determined spectroscopically. Figure 6 shows the diffuse reflectance UV-Vis spectra of the materials and Figure 6 inset shows the transformed Kubelka–Munk function as a function of the energy of light for the determination of the bandgap of the materials. All photocatalysts displayed narrower band-gap energies than P25, with values of 3.12 eV for TiO_2, 2.95 eV for TiO_2–GO, and 3.2 eV for P25. The increase in absorption at wavelength around 380 nm and mainly in the visible range is directly related to the interaction of TiO_2 and GO, the inherent light-absorbing ability of carbon materials, as well as to the electronic transitions between the carbons and phases of TiO_2, resulting in a lower band-gap (E_g= 2.95 eV, Table 2). The reduced band-gap in the TiO_2–GO material can be ascribed to the inherent light absorption capacity of carbon materials as well as to the electronic transitions between carbon and TiO_2 phases [19,35]

Table 2. BET surface area (S_{BET}), total pore volume (V_{pore}), pH at the point of zero charge (pH_{PZC}), crystallite size and band–gap energy (E_g) of materials of photocatalysts.

Catalyst	S_{BET} ($m^2\ g^{-1}$)	Vp ($cm^3\ g^{-1}$)	pH_{PZC}	Crystalline phase (%)	*Crystallite size (nm)*	E_g (eV)
P25	52		6.5	85 (A)*	22	3.20
TiO_2	118	0.11	3.5	100 (A)*	8	3.12
TiO_2–GO	120	0.17	3.0	100 (A)*	4	2.95

* A: anatase.

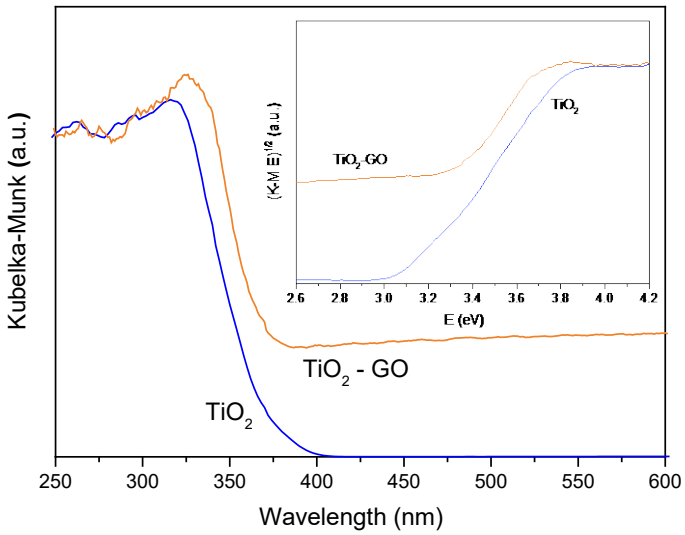

Figure 6. Diffuse reflectance UV–Vis spectra of TiO_2 and TiO_2-GO and plot of Kubelka–Munk units as a function of the light energy (inset).

3.2.2. Photocatalytic Performance of the Samples

The role of carbon materials in catalytic nitrate reduction is currently a field of high interest among researchers, being part of different types of catalyst for various processes. Gonzalez et al. [36] prepared Pd-Cu catalysts supported on ACs with different porosity for the removal of NO_3^- at room temperature under H_2 flow in batch reactors. The concluded that catalyst performance decreased as microporosity increased, favoring also the formation of NH_4^+. Sanchis et al. [37] modified the carbon surface by doping with N-species before preparing Pd-Sn catalysts, which were used in column

 doi:10.20944/preprints202508.1857.v1

under H_2-flow for the NO_3^- reduction. N-doping improved the catalysts performance by increasing conversion and decreasing the NH_4^+ selectivity. Both textural and chemical characteristics of carbon materials clearly influence the performance of the catalysts.

Carbon materials are also used in the development of electro-catalysts for the NO_3^- reduction with a high performance. Two main pathways are widely reported in the literature, likely, reduction to NH_4^+ [38] or reduction to N_2 [39].

Regarding the first route, the synthesis of NH_3, avoiding high temperatures, required the classical Haber–Bosch synthesis processes. Given the importance of NH_3 for the preparation of many compounds as well as for an energetic vector (H_2 carrier), the transformation of nitrates into ammonia is strongly justified. Doping TiO_2 with GO is more effective than doping with metals such as Co, as GO notably diminishes the initial potential of titania-based catalysts. The best performance, however, is achieved through co-doping with Co–GO. To improve the selectivity of the reduction of nitrate to nitrogen, the carbon support was doped with N-functionalities before the impregnation with two complementary metals (Pd-Cu) leading to the formation of Pd-N-N-Cu active structures. Intermediate $*NO_2$, *NO or *NH suggested that the reduction mechanism involves both deoxygenation and hydrogenation processes.

Researchers have investigated carbon materials for photocatalytic nitrate (NO_3^-) reduction, particularly biochars prepared from various biomasses such as straw, rapeseed, rice husk, softwood, and sewage sludge. These biochars have shown activity under UV irradiation, enabling the reduction of nitrates to NO_2 and NO [40]. Generally, the materials exhibit a low surface area (~30 $m^2 \cdot g^{-1}$) and a strongly basic character ($pH_pzc \approx 9.5$), though their composition varies significantly with the biomass precursor. Thus, biochar from sewage sludge contains a low ash content (below 2% wt.), while those produced from rice husk can exceed 45% wt.

In the absence of biochar the reduction of nitrate under UV-irradiation is negligible, as well as the performance of biochar in the dark, but high conversions are obtained catalyzed by biochar under UV-radiation. The presence of metal oxides in the ash content such as TiO_2, Al_2O_3 or Fe_2O_3 facilitate the reduction of adsorbed nitrates. Nitrates can be reduced on the carbon surface to NO_2 or forming nitrites that remain in solution according to the electron donor capacity of biochars. Subsequent photolysis of nitrites produces NO. Nevertheless, this process is only transferring pollution from the dissolution to the atmosphere and consequently should be optimized looking for selective processes producing preferentially N_2 as the only reaction product.

Developing photocatalysts involves the use of semiconductors, TiO_2 being the most widely applied despite its well-known limitations. Different strategies have been tried to overcome these lacks, starting by developing heterojunctions in the proper TiO_2 structure by inducing the formation of different crystalline phases looking for the synergism between phases. In such a basis, different studies were previously developed trying to improve the TiO_2 performance. Mohamed et al. [41] prepared mesoporous TiO_2 samples using different templates. These samples exhibited significant activity in photocatalytic NO_3^- reduction under UV irradiation, achieving conversion rates of 45–60%, in contrast to only 7% obtained with the benchmark P25. This improvement was associated with the role of mesoporosity, the formation of heterojunctions between the TiO_2 phases or the particle size, crystallite size having a decisive influence on the activity. Moreover, it is also presumed that such high activity is due to the presence of organic moieties acting as hole scavenger thus improving the catalytic performance. The formation of heterojunctions on TiO_2, active in the NO_3^- reduction, has been also systematically studied by doping with noble metals as Pd or other transition metals as Fe, Cu, Ag [42]. Results are influenced by factors as metal leaching and crystal size of doping agent, showing also in some cases a certain period of induction prior to the onset of nitrate removal.

Once demonstrated the good performance of both carbon and TiO_2 phases in the NO_3^- reduction, the direct conclusion is the preparation of carbon-TiO_2 composites looking also for the synergism between phases. However, and in spite that this combination is widely described for the treatment of many other pollutants, more specifically emerging pollutants [43], few references deals about the use of carbon-TiO_2 composites in the photocatalytic NO_3^- reduction.

 doi:10.20944/preprints202508.1857.v1

Shaban et al. [16] prepared C/TiO_2 photocatalysts by sol-gel procedure using glycine as carbon source. The E_g values decreased from 3.2 eV for undoped TiO_2 to 1.8 eV after doping with carbon, facilitating the NO_3^- reduction also under sunlight radiation. However, the reaction rate was lower compared with experiments carried out under UV-radiation. These catalysts are highly actives, reaching the total photocatalytic reduction of nitrates following a pseudo first-order reaction kinetics. Nitrites are observed as intermediate products with negligible formation of ammonia.

Among the different types of photocatalysts developed in our laboratories for environmental applications combining carbon materials and semiconductors [44-47], we selected GO. This choice was based on the significant band gap narrowing observed (Table 2) with the incorporation of only a small amount of dopant (4 wt% GO) in TiO_2-GO composites. These results are in good agreement to those exposed by Lin et al. [38]. Figure 5 shows the photocatalytic reduction profile of nitrate ion over the bare TiO_2, TiO_2–GO and P25 catalyst and experiment without catalyst (photolysis) at pH 2.5.

The NO_3^- reduction by photolysis is around 8% and the adsorption experiments (equilibrium) shows values around 3-5% of the initial NO_3^- concentration under dark conditions. The high photocatalytic activity of P25 regarding the bulk TiO_2 sample arises from the synergistic interaction between its anatase and rutile phases, as previously analyzed.

The incorporation of GO into TiO_2 also improved the photocatalytic characteristics of the TiO_2–GO composite, as clearly reflected in its superior performance, achieving even better results than the commercial P25 sample and enabling up to 80% nitrate removal within 1 hour. The observed differences may be attributed to the combined effects of TiO_2–GO lower band-gap energy, slightly reduced pH_{PZC}, and known photoluminescence quenching compared to bare TiO_2 [19,48,49]. Additionally, the presence of graphene derivatives appears to facilitate more efficient photo-generated electron transfer and suppress charge carrier recombination under solar radiation, possibly involving different photocatalytic mechanisms [50].

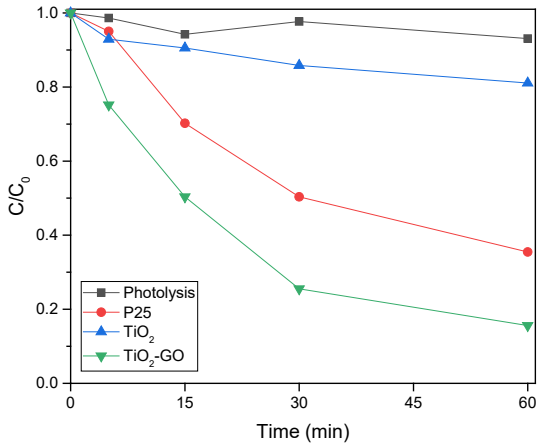

Figure 5. Photocatalytic degradation of NO_3^- as a function of time over P25, TiO_2 and TiO_2–GO catalysts at pH 2.5.

3.2.3. Influence of pH

As commented in the introduction section the reduction of NO_3^- strongly depends on the pH (equations 1 – 8). Nevertheless, the pH of solutions determines not only the reaction pathway through the ability of reactant (H^+) but also the charge either of the species in solutions and the catalysts surface. The catalysts surface becomes positively charged at pH values bellow the pH_{pzc} of catalysts, and negatively charged in more basic conditions, thus conditioning also the electrochemical interactions with the NO_3^- ions.

Figure 6 shows that pH and surface nature influence the photocatalytic performance of the samples. The increasing activity with increasing the acidity of solution is clear for both samples. Considering P25 (pH_{PZC} = 6.5, Table 2), at pH 2.5 about 60% of the nitrates are degraded in 1h, while at pH 10 only about 20% are degraded in the same period (Figure 6a). This effect is due to the fact

 doi:10.20944/preprints202508.1857.v1

that at acidic pH the TiO_2 surface is positively charged forming $TiOH_2^+$ species, facilitating the adsorption of nitrate ions (NO_3^-) to the active sites of the catalyst. On the contrary, at higher pH values, the surface of TiO_2 is negatively charged (TiO-) and as a consequence, the adsorption of nitrate ions is disadvantaged due to electrostatic repulsions. The mechanism of adsorption and degradation of NO_3^- on the TiO_2 surfaces was analysed by FTIR *in situ* experiments [13]. The NO_3^- is adsorbed on the Ti sites with the formation of $(M\text{-}O)_2{=}NO$ structures, which are converted to monodentate nitrite (M-O-N-O) as an intermediate reaction.

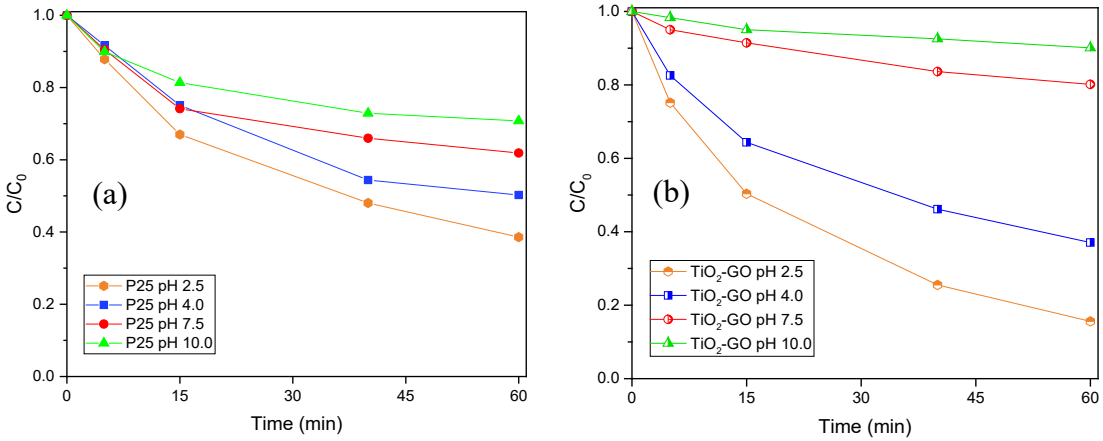

Figure 6. Effect of pH on the photoreduction of nitrate for **(a)** P25 and **(b)** TiO_2-GO under solar radiation.

In the case of TiO_2–GO (Figure 7b) a similar effect is observed and the highest nitrate degradation is observed at acidic pH values. Comparing the performance of P25 and TiO_2–GO across the pH range reveals the significant impact of surface chemistry modifications induced by the presence of GO. Under acidic conditions (pH < 4), the TiO_2–GO composite exhibits notably enhanced photocatalytic activity compared to P25. This improvement may be attributed to the increased formation of positively charged surface species, likely due to basic functional groups on the GO or electronic interactions between the GO and TiO_2 phases. However, under basic conditions (pH > 7.5), the opposite effect is observed. The TiO_2–GO composite becomes nearly inactive at pH 10, possibly due to the deprotonation of acidic functional groups on the GO surface or alterations in electron transfer dynamics between phases. The abundance of oxygen-containing surface groups (OSGs) on GO may contribute to the amphoteric behavior of the TiO_2–GO composite and influences charge transfer processes through intrinsic donor–acceptor interactions. As a result, the influence of pH on the TiO_2–GO composite is more pronounced than on P25. Hence, the superior photocatalytic activity of the TiO_2–GO composites relative to P25 can be attributed to strong interfacial interactions between TiO_2 and GO, facilitated by the oxygenated functional groups present on GO (such as epoxy and hydroxyl groups) [48]. These interactions promote optimal assembly and interfacial coupling during synthesis, resulting in GO platelets effectively embedded within the TiO_2 matrix, which enhances the overall photocatalytic performance of the TiO_2–GO composite under solar radiation [19,51].

3.2.4. Effect of hole Scavengers

As demonstrated in previous section, nitrates adsorbed on the TiO_2 surface can be photoreduced directly accepting electrons from conduction band. However, hole scavengers are commonly used to enhance photocatalytic reduction reactions [12,52]. The efficiency of the process being therefore related to the nature of the scavenger. In this study, the influence of ethanol, oxalic acid, and formic acid (0.08 M) on the performance of P25 and for TiO_2 and TiO_2-GO for the nitrate reduction at pH 2.5 is shown in Figures 7a and b, respectively. Product analysis confirmed that NH_4^+ was not detected under any conditions, regardless of reaction time, photocatalyst, or scavenger. As an example, Figure 7d shows the concentration of nitrate, nitrite and ammonium over TiO_2-GO catalyst using formic acid (0.08M). Small amounts of NO_2^- as intermediate were observed simultaneously with the decrease of

 doi:10.20944/preprints202508.1857.v1

nitrate concentration. After 60 min of reaction, no nitrogen-containing species remained in solution, indicating that nitrate could be completely reduced to N_2.

In the case of P25, the nitrate conversion after 1 hour of irradiation was approximately 60% in the absence of scavenger (Figure 7a). As expected, the addition of scavengers enhanced nitrate conversion, following the trend: ethanol < oxalic acid < formic acid. This effect can be due to the enhanced separation of electrons and holes and/or the generation of reductive carboxyl anion radicals ($CO_2^{\bullet-}$) during the decomposition of the hole scavenger [52]. These radicals have strong reductive potential ($E°(CO_2/CO_2^{\bullet-})$ = –1.8 V for converting nitrate to nitrite ($E°(NO_3^-/NO_2^-)$ = 0.94 V), to N_2 ($E°(NO_3^-/N_2)$ = 1.25 V), and for nitrite to N_2 ($E°(NO_2^-/N_2)$ = 1.45 V) [42,53].

The effect of the initial concentration of formic acid (HCOOH, 0.04, 0.08 and 0.012 M) was also evaluated on the nitrate reduction (Figure 7c). It was found that the reduction rate of nitrate enhanced with the increase in formic acid concentration from 0.04 to 0.08 M, although an increase to 0.12M leads to a decrease in the photoreduction indicating overdosing. A similar trend has been observed in other photocatalytic systems [54]. Shi et al. develops Z-scheme ZnSe/ $BiVO_4$ has high selective photocatalysts of NO_3^- into N_2. They used formic acid, ethanol and acetic acid as scavengers. The best performance was obtained with formic acid, which was attributed to the simultaneous apportioning of H^+ and $CO_2^{\bullet-}$ radicals. These findings highlight the critical role of acid concentration: insufficient H^+ availability at low formic acid concentrations slows the reaction and favors NO_2^- formation, whereas excessive concentrations promote NH_4^+ formation. Therefore, identifying the optimal formic acid concentration is essential for maximizing nitrate reduction efficiency.

When anatase-based photocatalysts are used, the performance of TiO_2 and TiO_2-GO composite is enhanced by the presence of formic acid, although the increase in activity is not as significant as in the case of P25 (Figure 7b). In the absence of a scavenger, the conversion of nitrates on P25 and TiO_2-GO was 60% and 80%, respectively, after 1 h of reaction (Figures 7a and b, respectively). This difference is progressively attenuated with an increasing concentration of formic acid in solution (Figure 7c), to the extent that the performance of both materials is quite similar at 0.08 M. However, the performance of TiO_2-GO is lower than that of P25 at a higher concentration (0.12 M) of formic acid.

Furthermore, it was observed that the highest performance of the TiO_2–GO composite was not achieved with formic acid, but with oxalic acid. Complete nitrate conversion was achieved in just 15 minutes when TiO_2-GO was used with oxalic acid as the scavenger. These are the best experimental conditions observed throughout this series of experiments, which again demonstrate the strong influence of interactions between NO_3^-, the scavenger and the catalyst surface on the final conversion and selectivity achieved. Considering the stronger effect of pH on the performance of this sample regarding P25 (Figure 6), the superior performance of oxalic acid compared to formic acid can be attributed to the greater acid strength of oxalic acid (pKa = 1.2) compared to formic acid (pKa = 3.8).

Different studies have used oxalic acid as a scavenger for NO_3^- reduction. For example, Li et al. [55] analysed the photoreduction of nitrates by oxalic acid at pH 2.4. They concluded that the reaction was accelerated by the scavenger and that there was an optimal concentration. Oxalic acid is adsorbed onto the TiO_2 surface, forming oxalate complexes. However, in excess, oxalic acid occupies all surface sites, which hinders the adsorption of nitrates and thus decreases conversion. The reaction involves the formation of $HNO_3^{\bullet-}$ and $C_2O_4^{\bullet-}$ radicals, which decompose to $CO_2^{\bullet-}$, and the main reaction product is ammonia. Oxalic acid acts as a sacrificial electron donor.

Nevertheless, our results are more consistent with those reported by Sowmya et al. [56]. They found that the reaction on TiO_2-Ag depends on the oxalic acid concentration, which is oxidised following a pseudo-first-order kinetic. NH_4^+ was not detected, and NO_2^- was only observed at short reaction times (Figure 7d). Clearly, doping with either Ag or GO significantly affects the nature of the interactions between the reactants and catalysts. This results in a decreased BG value and improved charge separation, changing not only the conversion values, but also the reaction pathway and product distribution compared to results obtained with bare TiO_2.

 doi:10.20944/preprints202508.1857.v1

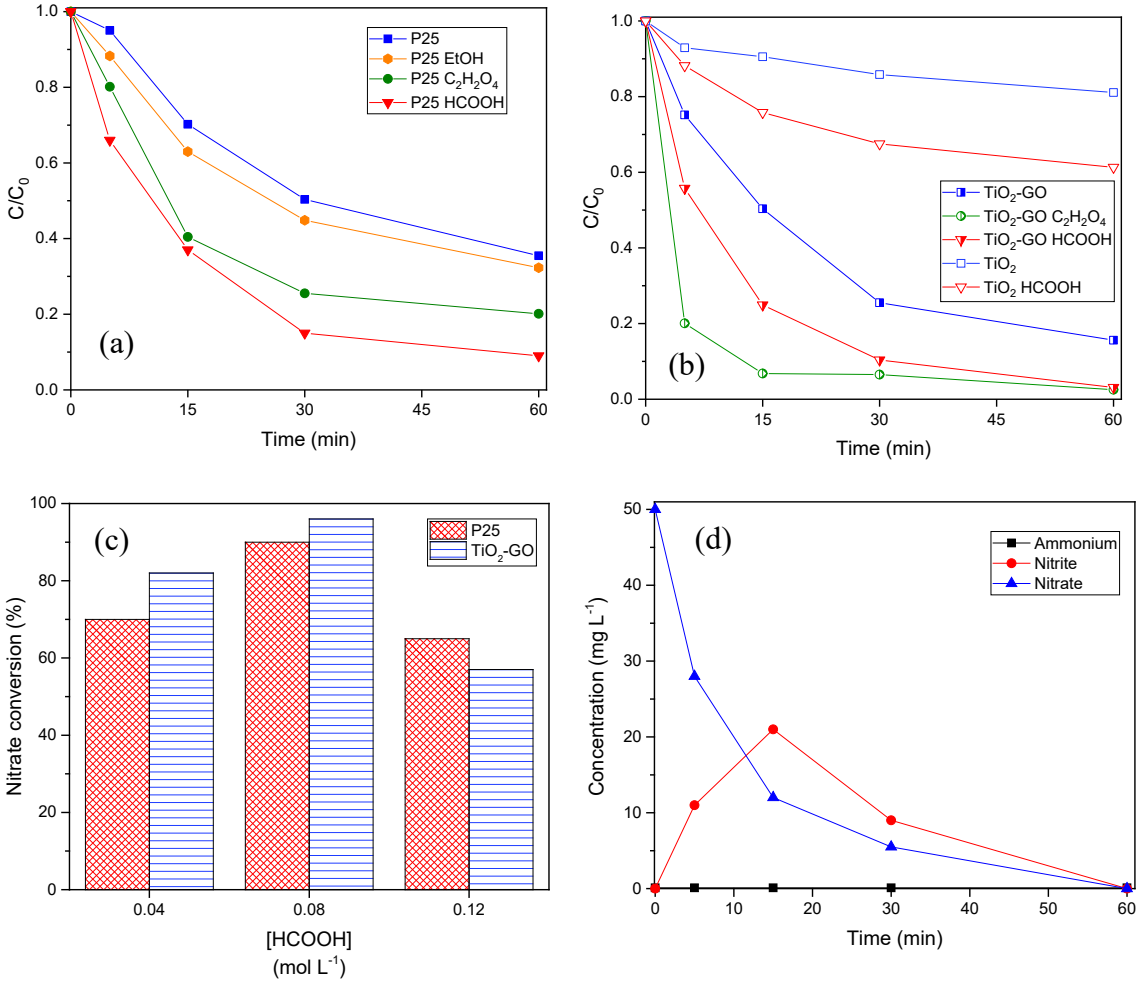

Figure 7. Effect of hole scavengers (0.08M) on the photoreduction of nitrate for **(a)** P25 and **(b)** TiO_2-GO at pH 2.5 under solar radiation; **(c)** Effect of the initial concentration of formic acid on the nitrate reduction; (**d**) Nitrate, nitrite and ammonium concentration over TiO_2-GO catalyst using formic acid (0.08M) at pH 2.5.

4. Conclusions

This study highlights the significant influence of carbon support properties, photocatalyst composition, pH, and the presence of hole scavengers on the efficiency of nitrate removal from aqueous solutions using *E. coli* biofilms and photocatalysis. Among the carbon materials tested, carbon aerogels (CA) exhibited the best performance as biofilm supports, due to their mesoporous structure, low ash content, and slightly acidic surface character, which favor bacterial adhesion and activity. The presence of oxygenated surface groups on CA further promoted the formation of structured and active biofilm colonies. In contrast, activated carbons (ACs), particularly the commercial sample N, showed lower performance, likely due to their compact microporous structure, higher ash content, and less favorable surface chemistry

In the photocatalytic study, TiO_2–GO composites outperformed commercial P25 under acidic conditions, achieving up to 80% nitrate degradation in 1 hour, and even complete removal in 15 minutes with oxalic acid as a scavenger. The synergistic effects between TiO_2 and GO contributed to enhanced charge separation, increased formation of active surface species, and improved light absorption. However, the composite was more sensitive to experimental conditions such as pH and scavenger concentration, showing strong deactivation under overdosing or at high pH values. The combined results demonstrate that tailoring the textural and chemical properties of supports and photocatalysts is key to optimizing nitrate removal performance.

 doi:10.20944/preprints202508.1857.v1

Author Contributions: Conceptualization, L.M.P.-M and S.M.-T.; methodology, F.J.M.-H. and S.M.-T.; investigation, L.M.P.-M. and S.M.-T.; writing—original draft preparation, L.M.P.-M. and S.M.-T.; writing—review and editing, L.M.P.-M., F.J.M.-H and S.M.-T.; supervision, F.J.M.-H.; funding acquisition, L.M.P.-M., S.M.-T. and F.J.M.-H. All authors have read and agreed to the published version of the manuscript.

Funding: This work was financially supported by projects with ref. PID2021–126579OB-C31 by MICIU/AEI/10.13039/501100011033 and ERDF "A way of making Europe" and by Junta de Andalucía - Consejería de Universidad, Investigación e Innovación - Project P21_00208150

Acknowledgments: S.M.-T. is grateful to MICIN/AEI/10.13039/501100011033 and FSE "El FSE invierte en tu futuro" for the Ramon y Cajal (RYC-2019-026634-I) research contract. "Unidad de Excelencia Química Aplicada a Biomedicina y Medioambiente" of the University of Granada (UEQ-UGR) is gratefully acknowledged for the technical assistance.

Conflicts of Interest: The authors declare no conflict of interest.

References

1. Gómez-Jakobsen, F.; Ferrera, I.; Yebra, L.; Mercado, J.M. Two decades of satellite surface chlorophyll a concentration (1998–2019) in the Spanish Mediterranean marine waters (Western Mediterranean Sea): Trends, phenology and eutrophication assessment. *Remote Sensing Applications: Society and Environment* **2022**, *28*, 100855, doi:https://doi.org/10.1016/j.rsase.2022.100855.
2. Directive (EU) 2020/2184 of the European Parliament and of the Council of 16 December 2020 on the quality of water intended for human consumption (recast) (Text with EEA relevance). Availabe online: https://eur-lex.europa.eu/eli/dir/2020/2184/oj (accessed on
3. Zhang, T.; Xu, Q.; Liu, X.; Lei, Q.; Luo, J.; An, M.; Du, X.; Qiu, W.; Zhang, X.; Wang, F., et al. Sources, fate and influencing factors of nitrate in farmland drainage ditches of the irrigation area. *Journal of Environmental Management* **2024**, *367*, 122113, doi:https://doi.org/10.1016/j.jenvman.2024.122113.
4. Ateunkeng, J.G.; Boum, A.T.; Bitjoka, L. A binary-level hybrid intelligent control configuration for sustainable energy consumption in an activated sludge biological wastewater treatment plant. *Journal of Water Process Engineering* **2024**, *65*, 105902, doi:https://doi.org/10.1016/j.jwpe.2024.105902.
5. Zhu, G.-C.; Lu, Y.-Z.; Xu, L.-R. Effects of the carbon/nitrogen (C/N) ratio on a system coupling simultaneous nitrification and denitrification (SND) and denitrifying phosphorus removal (DPR). *Environmental Technology* **2021**, *42*, 3048-3054, doi:10.1080/09593330.2020.1720310.
6. Lago, A.; Rocha, V.; Barros, O.; Silva, B.; Tavares, T. Bacterial biofilm attachment to sustainable carriers as a clean-up strategy for wastewater treatment: A review. *Journal of Water Process Engineering* **2024**, *63*, 105368, doi:https://doi.org/10.1016/j.jwpe.2024.105368.
7. Ardiati, F.C.; Anita, S.H.; Nurhayat, O.D.; Chempaka, R.M.; Yanto, D.H.Y.; Watanabe, T.; Wilén, B.-M. Evaluation of batch and fed-batch rotating drum biological contactor using immobilized Trametes hirsuta EDN082 for non-sterile real textile wastewater treatment. *Journal of Environmental Chemical Engineering* **2024**, *12*, 113241, doi:https://doi.org/10.1016/j.jece.2024.113241.
8. Barrabés, N.; Sá, J. Catalytic nitrate removal from water, past, present and future perspectives. *Applied Catalysis B: Environmental* **2011**, *104*, 1-5, doi:https://doi.org/10.1016/j.apcatb.2011.03.011.
9. Cai, W.; Chen, C.; Bao, C.; Gu, J.-n.; Li, K.; Jia, J. Nitrate reduction to nitrogen in wastewater using mesoporous carbon encapsulated Pd–Cu nanoparticles combined with in-situ electrochemical hydrogen evolution. *Journal of Environmental Management* **2024**, *362*, 121346, doi:https://doi.org/10.1016/j.jenvman.2024.121346.
10. Kudo, A.; Domen, K.; Maruya, K.-i.; Onishi, T. Photocatalytic Reduction of NO3− to Form NH3 over Pt–TiO2. *Chemistry Letters* **1987**, *16*, 1019-1022, doi:10.1246/cl.1987.1019.
11. Pintar, A.; vetinc, M.; Levec, J. Hardness and Salt Effects on Catalytic Hydrogenation of Aqueous Nitrate Solutions. *Journal of Catalysis* **1998**, *174*, 72-87, doi:https://doi.org/10.1006/jcat.1997.1960.
12. Soares, O.S.G.P.; Pereira, M.F.R.; Órfão, J.J.M.; Faria, J.L.; Silva, C.G. Photocatalytic nitrate reduction over Pd–Cu/TiO2. *Chemical Engineering Journal* **2014**, *251*, 123-130, doi:https://doi.org/10.1016/j.cej.2014.04.030.

13. Bahadori, E.; Compagnoni, M.; Tripodi, A.; Freyria, F.; Armandi, M.; Bonelli, B.; Ramis, G.; Rossetti, I. Photoreduction of nitrates from waste and drinking water. *Materials Today: Proceedings* **2018**, *5*, 17404-17413, doi:https://doi.org/10.1016/j.matpr.2018.06.042.
14. Zhao, X.; Zhang, G.; Zhang, Z. TiO2-based catalysts for photocatalytic reduction of aqueous oxyanions: State-of-the-art and future prospects. *Environment International* **2020**, *136*, 105453, doi:https://doi.org/10.1016/j.envint.2019.105453.
15. Qin, J.; Liu, N.; Wei, Y.; Lu, Y.; Huang, Y.; Zhao, Q.; Ye, Z. The mechanism of efficient photoreduction nitrate over anatase TiO2 in simulated sunlight. *Chemosphere* **2022**, *307*, 135921, doi:https://doi.org/10.1016/j.chemosphere.2022.135921.
16. Shaban, Y.A.; El Maradny, A.A.; Al Farawati, R.K. Photocatalytic reduction of nitrate in seawater using C/TiO2 nanoparticles. *Journal of Photochemistry and Photobiology A: Chemistry* **2016**, *328*, 114-121, doi:https://doi.org/10.1016/j.jphotochem.2016.05.018.
17. Morales-Torres, S.; Maldonado-Hódar, F.J.; Pérez-Cadenas, A.F.; Carrasco-Marín, F. Textural and mechanical characteristics of carbon aerogels synthesized by polymerization of resorcinol and formaldehyde using alkali carbonates as basification agents. *Physical Chemistry Chemical Physics* **2010**, *12*, 10365-10372, doi:10.1039/C003396K.
18. Hummers Jr, W.S.; Offeman, R.E. Preparation of graphitic oxide. *Journal of the american chemical society* **1958**, *80*, 1339.
19. Pastrana-Martínez, L.M.; Morales-Torres, S.; Likodimos, V.; Figueiredo, J.L.; Faria, J.L.; Falaras, P.; Silva, A.M.T. Advanced nanostructured photocatalysts based on reduced graphene oxide-TiO_2 composites for degradation of diphenhydramine pharmaceutical and methyl orange dye. *Applied Catalysis B: Environmental* **2012**, *123-124*, 241-256, doi:https://doi.org/10.1016/j.apcatb.2012.04.045.
20. Brunauer, S.; Emmett, P.H.; Teller, E. Adsorption of gases in multimolecular layers. *Journal of the American Chemical Society* **1938**, *60*, 309-319.
21. Bansal, R.C.; Donnet, J.B.; Stoeckli, F. *Active Carbon*; Bansal, R.C., Donnet, J.B., Stoeckli, F., Eds.; Marcel Dekker: New York, 1988.
22. Barrett, E.P.; Joyner, L.G.; Halenda, P.P. The Determination of Pore Volume and Area Distributions in Porous Substances. I. Computations from Nitrogen Isotherms. *Journal of the American Chemical Society* **1951**, *73*, 373-380, doi:10.1021/ja01145a126.
23. Leon y Leon, C.A.; Solar, J.M.; Calemma, V.; Radovic, L.R. Evidence for the protonation of basal plane sites on carbon. *Carbon* **1992**, *30*, 797-811, doi:http://dx.doi.org/10.1016/0008-6223(92)90164-R.
24. Kesserű, P.; Kiss, I.; Bihari, Z.; Polyák, B. Investigation of the denitrification activity of immobilized Pseudomonas butanovora cells in the presence of different organic substrates. *Water Research* **2002**, *36*, 1565-1571, doi:https://doi.org/10.1016/S0043-1354(01)00364-5.
25. Lin, C.; Ritter, J.A. Effect of synthesis pH on the structure of carbon xerogels. *Carbon* **1997**, *35*, 1271-1278, doi:https://doi.org/10.1016/S0008-6223(97)00069-9.
26. Karanasios, K.A.; Vasiliadou, I.A.; Pavlou, S.; Vayenas, D.V. Hydrogenotrophic denitrification of potable water: A review. *Journal of Hazardous Materials* **2010**, *180*, 20-37, doi:https://doi.org/10.1016/j.jhazmat.2010.04.090.
27. Reguera, G.; McCarthy, K.D.; Mehta, T.; Nicoll, J.S.; Tuominen, M.T.; Lovley, D.R. Extracellular electron transfer via microbial nanowires. *Nature* **2005**, *435*, 1098-1101, doi:10.1038/nature03661.
28. Loosdrecht, M.C.v.; Lyklema, J.; Norde, W.; Schraa, G.; Zehnder, A.J. Electrophoretic mobility and hydrophobicity as a measured to predict the initial steps of bacterial adhesion. *Applied and Environmental Microbiology* **1987**, *53*, 1898-1901, doi:doi:10.1128/aem.53.8.1898-1901.1987.
29. Renner, L.D.; Weibel, D.B. Physicochemical regulation of biofilm formation. *MRS Bulletin* **2011**, *36*, 347-355, doi:10.1557/mrs.2011.65.
30. Bautista-Toledo, M.I.; Maldonado-Hódar, F.J.; Morales-Torres, S.; Pastrana-Martínez, L.M. Supported Biofilms on Carbon–Oxide Composites for Nitrate Reduction in Agricultural Waste Water. *Molecules* **2021**, *26*, 2987.
31. Maldonado-Hódar, F.J. Advances in the development of nanostructured catalysts based on carbon gels. *Catalysis Today* **2013**, *218-219*, 43-50, doi:https://doi.org/10.1016/j.cattod.2013.06.005.

 doi:10.20944/preprints202508.1857.v1

32. Maldonado-Hódar, F.J.; Morales-Torres, S.; Ribeiro, F.; Silva, E.R.; Pérez-Cadenas, A.F.; Carrasco-Marín, F.; Oliveira, F.A.C. Development of Carbon Coatings for Cordierite Foams: An Alternative to Cordierite Honeycombs. *Langmuir* **2008**, *24*, 3267-3273, doi:10.1021/la703217t.
33. Paritosh, K.; Kesharwani, N. Biochar mediated high-rate anaerobic bioreactors: A critical review on high-strength wastewater treatment and management. *Journal of Environmental Management* **2024**, *355*, 120348, doi:https://doi.org/10.1016/j.jenvman.2024.120348.
34. Zhang, S.; Hu, X.; Su, J.; Wang, J.; Ali, A.; Qian, K.; Wu, X. Modified biochar improved simultaneous nitrate removal and soluble microbial products regulation in low carbon wastewater: Insights from the biocarrier and community function. *Journal of Water Process Engineering* **2024**, *65*, 105762, doi:https://doi.org/10.1016/j.jwpe.2024.105762.
35. Silva, C.G.; Faria, J.L. Photocatalytic oxidation of benzene derivatives in aqueous suspensions: Synergic effect induced by the introduction of carbon nanotubes in a TiO_2 matrix. *Applied Catalysis B: Environmental* **2010**, *101*, 81-89, doi:http://dx.doi.org/10.1016/j.apcatb.2010.09.010.
36. González, D.T.; Baeza, J.A.; Alemany-Molina, G.; Calvo, L.; Gilarranz, M.A.; Morallón, E.; Cazorla-Amorós, D. Catalytic nitrate reduction using a Pd-Cu catalysts supported on carbon materials with different porous structure. *Journal of Environmental Chemical Engineering* **2025**, *13*, 115979, doi:https://doi.org/10.1016/j.jece.2025.115979.
37. Sanchis, I.; Rodriguez, J.J.; Mohedano, A.F.; Diaz, E. N-doped activated carbon as support of Pd-Sn bimetallic catalysts for nitrate catalytic reduction. *Catalysis Today* **2023**, *423*, 114011, doi:https://doi.org/10.1016/j.cattod.2023.01.018.
38. Lin, P.; Chen, R.; Xu, S.; Xia, X.; Zhao, F.; Ren, X.; Lu, Y.; Gao, L.; Bao, J.; Liu, A. Efficient Co and GO co-doped TiO_2 catalysts for the electrochemical reduction of nitrate to ammonia. *Catalysis Science & Technology* **2025**, *15*, 1445-1455, doi:10.1039/D4CY01228C.
39. Zhang, J.; Xia, H.; Jiang, K.; Chen, X.; Liu, C.; Yin, X.; Liu, Y.; Xu, H.; Yang, W. High-efficiency nitrate reduction to nitrogen using PdCu dual-atom electrocatalysts anchored on nitrogen-doped carbon. *Chemical Engineering Journal* **2025**, *519*, 165362, doi:https://doi.org/10.1016/j.cej.2025.165362.
40. Zhou, L.; Richard, C.; Ferronato, C.; Chovelon, J.-M.; Sleiman, M. Investigating the performance of biomass-derived biochars for the removal of gaseous ozone, adsorbed nitrate and aqueous bisphenol A. *Chemical Engineering Journal* **2018**, *334*, 2098-2104, doi:https://doi.org/10.1016/j.cej.2017.11.145.
41. Mohamed, M.M.; Asghar, B.H.M.; Muathen, H.A. Facile synthesis of mesoporous bicrystallized TiO_2(B)/anatase (rutile) phases as active photocatalysts for nitrate reduction. *Catalysis Communications* **2012**, *28*, 58-63, doi:https://doi.org/10.1016/j.catcom.2012.08.012.
42. Sá, J.; Agüera, C.A.; Gross, S.; Anderson, J.A. Photocatalytic nitrate reduction over metal modified TiO_2. *Applied Catalysis B: Environmental* **2009**, *85*, 192-200, doi:https://doi.org/10.1016/j.apcatb.2008.07.014.
43. Pérez-Molina, Á.; Morales-Torres, S.; Maldonado-Hódar, F.J.; Pastrana-Martínez, L.M. Functionalized Graphene Derivatives and TiO2 for High Visible Light Photodegradation of Azo Dyes. *Nanomaterials* **2020**, *10*, 1106.
44. Pérez-Poyatos, L.T.; Pastrana-Martínez, L.M.; Morales-Torres, S.; Maldonado-Hódar, F.J. Novel strategies to develop efficient carbon/TiO2 photocatalysts for the total mineralization of VOCs in air flows: Improved synergism between phases by mobile N-, O- and S-functional groups. *Chemical Engineering Journal* **2025**, *508*, 160986, doi:https://doi.org/10.1016/j.cej.2025.160986.
45. Pérez-Molina, Á.; Morales-Torres, S.; Maldonado-Hódar, F.J.; Pastrana-Martínez, L.M. Functionalization of graphitic carbon nitride/ZnO heterojunctions with zinc cyanamide groups: A powerful approach for photocatalytic degradation of anticancer drugs. *Separation and Purification Technology* **2025**, *364*, 132306, doi:https://doi.org/10.1016/j.seppur.2025.132306.
46. Regadera-Macías, A.M.; Morales-Torres, S.; Pastrana-Martínez, L.M.; Maldonado-Hódar, F.J. Ethylene removal by adsorption and photocatalytic oxidation using biocarbon –TiO_2 nanocomposites. *Catalysis Today* **2023**, *413-415*, 113932, doi:https://doi.org/10.1016/j.cattod.2022.10.014.
47. Mirikaram, N.; Pérez-Molina, Á.; Morales-Torres, S.; Salemi, A.; Maldonado-Hódar, F.J.; Pastrana-Martínez, L.M. Photocatalytic Perfomance of ZnO-Graphene Oxide Composites towards the Degradation of Vanillic Acid under Solar Radiation and Visible-LED. *Nanomaterials* **2021**, *11*, 1576.

 doi:10.20944/preprints202508.1857.v1

48. Pastrana-Martínez, L.M.; Morales-Torres, S.; Likodimos, V.; Falaras, P.; Figueiredo, J.L.; Faria, J.L.; Silva, A.M.T. Role of oxygen functionalities on the synthesis of photocatalytically active graphene–TiO_2 composites. *Applied Catalysis B: Environmental* **2014**, *158-159*, 329-340, doi:https://doi.org/10.1016/j.apcatb.2014.04.024.
49. Morales-Torres, S.; Pastrana-Martínez, L.M.; Figueiredo, J.L.; Faria, J.L.; Silva, A.M.T. Design of graphene-based TiO2 photocatalysts-a review. *Environmental Science and Pollution Research* **2012**, *19*, 3676-3687, doi:10.1007/s11356-012-0939-4.
50. Fan, W.; Lai, Q.; Zhang, Q.; Wang, Y. Nanocomposites of TiO_2 and Reduced Graphene Oxide as Efficient Photocatalysts for Hydrogen Evolution. *The Journal of Physical Chemistry C* **2011**, *115*, 10694-10701, doi:10.1021/jp2008804.
51. Sampaio, M.J.; Silva, C.G.; Silva, A.M.T.; Pastrana-Martínez, L.M.; Han, C.; Morales-Torres, S.; Figueiredo, J.L.; Dionysiou, D.D.; Faria, J.L. Carbon-based TiO_2 materials for the degradation of Microcystin-LA. *Applied Catalysis B: Environmental* **2015**, *170-171*, 74-82, doi:https://doi.org/10.1016/j.apcatb.2015.01.013.
52. Li, L.; Xu, Z.; Liu, F.; Shao, Y.; Wang, J.; Wan, H.; Zheng, S. Photocatalytic nitrate reduction over Pt–Cu/TiO_2 catalysts with benzene as hole scavenger. *Journal of Photochemistry and Photobiology A: Chemistry* **2010**, *212*, 113-121, doi:https://doi.org/10.1016/j.jphotochem.2010.04.003.
53. Stanbury, D.M. Reduction Potentials Involving Inorganic Free Radicals in Aqueous Solution. In *Advances in Inorganic Chemistry*, Sykes, A.G., Ed. Academic Press: 1989; Vol. 33, pp. 69-138.
54. Shi, H.; Li, C.; Wang, L.; Wang, W.; Bian, J.; Meng, X. Photocatalytic reduction of nitrate pollutants by novel Z-scheme ZnSe/BiVO4 heterostructures with high N2 selectivity. *Separation and Purification Technology* **2022**, *300*, 121854, doi:https://doi.org/10.1016/j.seppur.2022.121854.
55. Li, Y.; Wasgestian, F. Photocatalytic reduction of nitrate ions on TiO_2 by oxalic acid. *Journal of Photochemistry and Photobiology A: Chemistry* **1998**, *112*, 255-259, doi:https://doi.org/10.1016/S1010-6030(97)00293-1.
56. Sowmya, A.; Meenakshi, S. Photocatalytic reduction of nitrate over Ag–TiO_2 in the presence of oxalic acid. *Journal of Water Process Engineering* **2015**, *8*, e23-e30, doi:https://doi.org/10.1016/j.jwpe.2014.11.004.